crystals

MDPI

Article

Structural Characterization and Dynamics of a Layered 2D Perovskite $[NH_3(CH_2)_5NH_3]MnCl_4$ Crystal near Phase Transition Temperature

Ae Ran Lim [1,2,*] and Yeji Na [1]

[1] Graduate School of Carbon Convergence Engineering, Jeonju University, Jeonju 55069, Korea
[2] Department of Science Education, Jeonju University, Jeonju 55069, Korea
* Correspondence: aeranlim@hanmail.net

Abstract: $[NH_3(CH_2)_5NH_3]MnCl_4$ crystals are grown via slow evaporation, and the crystal undergoes a phase transition at 298 K (T_C) according to differential scanning calorimetry, and the structures determined via X-ray diffraction at 173 and 333 K are orthorhombic systems in the space group Imma. These results differed slightly from those previously reported, and the reasons for this are analyzed. The thermal stability is relatively high, with a thermal decomposition temperature of approximately 570 K. The ^1H spin-lattice relaxation times $t_{1\rho}$ exhibited very large variations, as indicated by the large thermal displacement around the ^1H atoms, suggesting energy transfer at ~T_C, even if no structural changes occurred. The influences of the chemical shifts of ^1H of NH_3 and short $t_{1\rho}$ of C1 adjacent to NH_3 in cation are insignificant, indicating a minor change in the N−H···Cl hydrogen bond related to the coordination geometry of the $MnCl_6$ octahedron. These properties will be make it a potential application for eco-friendly solar cells.

Keywords: crystal structure; organic–inorganic hybrid; $[NH_3(CH_2)_5NH_3]MnCl_4$; phase transition; nuclear magnetic resonance; thermodynamic properties

Citation: Lim, A.R.; Na, Y. Structural Characterization and Dynamics of a Layered 2D Perovskite $[NH_3(CH_2)_5NH_3]MnCl_4$ Crystal near Phase Transition Temperature. *Crystals* **2022**, *12*, 1298. https://doi.org/10.3390/cryst12091298

Academic Editor: Luisa De Marco

Received: 29 July 2022
Accepted: 12 September 2022
Published: 14 September 2022

1. Introduction

Hybrid perovskite compounds are of scientific interest because of the diversity of their crystal structures, which govern their structural dynamics and ferroelastic and thermodynamic properties. In addition, ferroelasticity is commonly observed in compounds with perovskite crystal structures, and the ferroelastic twin domains in organic–inorganic hybrid perovskites attract much attention [1–6]. The organic cation of the hybrid material contributes to properties such as structural flexibility and optical characteristics, whereas the inorganic anion is responsible for the thermal and mechanical properties [7,8]. Moreover, the fabrication of hybrid perovskites was recently reported as a major challenge in the context of developing ferroelastic semiconductors [9]. Furthermore, successful hybrid perovskite ferroelectric performances render hybrid perovskites suitable candidates for use in flexible and wearable devices [10,11]. Additionally, solar cells based on $CH_3NH_3PbX_3$ (X = Cl, Br, or I) organic–inorganic hybrid compounds recently attracted interest. However, perovskites containing Pb are toxic and decompose in humid air, and thus, developing alternative green hybrid perovskite solar cells is necessary [4–6,12–16]. Hence, detailed characterizations of perovskite structures and the dynamics of novel organic–inorganic hybrid compounds $[NH_3(CH_2)_nNH_3]MX_4$ (n = 2, 3, 4, . . . , M^{II} is a transition metal, such as Mn, Fe, or Cu, and X is a halogen ion), which crystallize in perovskite-type layer structures in various configurations, are increasingly necessary due to their potential applications as green alternatives. The diammonium hybrid perovskites $[NH_3(CH_2)_nNH_3]BX_4$, with one-dimensional (0D) and two-dimensional (2D) structures, have been extensively investigated [17–30]. In the case of B = Mn, Cu, and Cd, the crystal structures consist of an alternate octahedrally coordinated $(BX_6)^{2-}$ and organic cations. In the case of B = Co and

Zn, isolated tetrahedral $(BX_4)^{2-}$ is coordinated between the organic cations [31,32]. These 2D hybrid perovskite types have various potential applications in electrochemical devices such as chemical sensors, supercapacitors, batteries, and solar cells [17,24,25,33].

Layered 2D hybrid perovskite $[NH_3(CH_2)_5NH_3]MnCl_4$ crystals (n = 5, M = Mn, and X = Cl) comprise organic and inorganic ions. The organic $[NH_3(CH_2)_5NH_3]^{2+}$ cations and inorganic $[MnCl_4]^{2-}$ anions are alternately stacked along the longest axis, with the inorganic layer extended via corner-shared octahedra. The organic and inorganic layers are interconnected by N−H···Cl hydrogen bonds [23]. The phase transition associated with the order–disorder transition between two orthorhombic phases is from Pnma to Imma at 299.6 K (= phase transition temperature T_C) [31]. The lattice constants at 298 K reported by Mondal et al. [23] are a = 7.1742 Å, b = 7.3817 Å, c = 23.9650 Å, and Z = 4. The crystal structure at 298 K is shown in Figure 1 (CCDC 1401387) [23], with each layer of alkylenediammonium chains inserted between two infinite sheets of corner-sharing $MnCl_6$ octahedra.

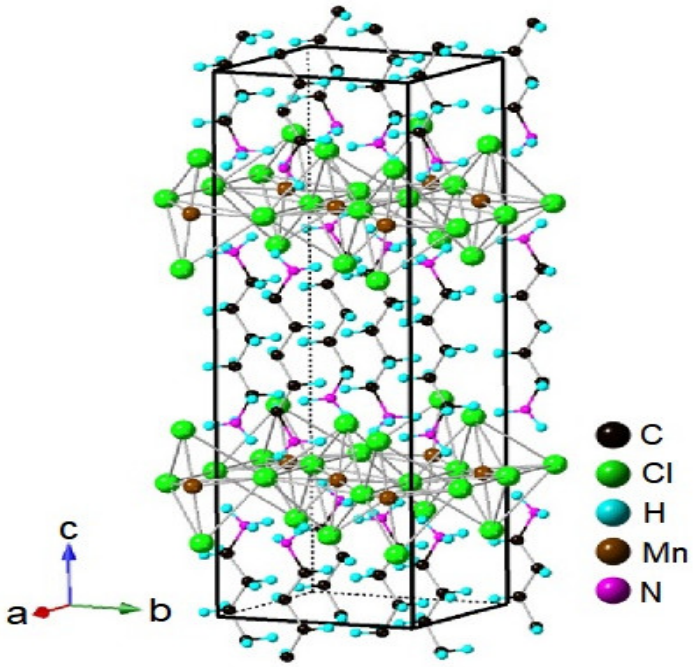

Figure 1. Orthorhombic structure of a $[NH_3(CH_2)_5NH_3]MnCl_4$ crystal at 298 K [23].

Research regarding $[NH_3(CH_2)_5NH_3]MnCl_4$ was initially published by Arend et al. [34,35], mainly as research reports regarding the crystal structure and T_C of 299.6 K based on the heat capacity. Based on recent results, Mondal et al. [23] studied the crystallographic characteristics of this crystal, with Lv et al. [36] reporting the dielectric and photoluminescence characteristics.

In this study, $[NH_3(CH_2)_5NH_3]MnCl_4$ single crystals were grown using an aqueous solution-based method, and T_C was confirmed using differential scanning calorimetry (DSC). In addition, the structures of the crystals below T_C and above T_C were confirmed using single-crystal X-ray diffraction (XRD). The thermodynamic properties were investigated as a function of temperature. Finally, the structural dynamics of the $[NH_3(CH_2)_5NH_3]^{2+}$ cation at ~T_C were analyzed using nuclear magnetic resonance (NMR) chemical shifts and spin-lattice relaxation times $t_{1\rho}$. The physicochemical properties of $[NH_3(CH_2)_5NH_3]MnCl_4$ without structural changes at ~T_C should render its use in proton conductors viable.

2. Materials and Methods

Single crystals of perovskite-type $[NH_3(CH_2)_5NH_3]MnCl_4$ were grown via slow evaporation from an aqueous solution containing $NH_2(CH_2)_5NH_2{\cdot}2HCl$ (98%, Sigma-Aldrich, St. Louis, MO, USA) and $MnCl_2$ (98%, Sigma-Aldrich). The mixture was stirred and heated,

the resulting solution was filtered, and light-yellow single crystals were obtained after five weeks in a constant-temperature bath at 300 K.

Fourier transform infrared (FT-IR) spectra were measured between 4000 and 500 cm^{-1} using an L1600300 spectrometer (PerkinElmer, Waltham, MA, USA) and compressed KBr pellets.

DSC (DSC 25, TA Instruments, New Castle, DE, USA) was performed to observe the structural phase transitions by heating in the temperature range 200–480 K at 10 K min^{-1} under N_2 gas. Thermogravimetric analysis (TGA) was performed using a thermogravimetric analyzer (TA Instruments) in the temperature range 300–870 K at the same heating rate.

The lattice parameters at various temperatures were determined via single-crystal XRD at the Western Seoul Center of the Korea Basic Science Institute. A crystal was lifted in paratone oil and mounted in a D8 Venture diffractometer (Bruker, Billerica, MA, USA) equipped with a Mo-Kα radiation source, PHOTON III M14 detector (Bruker), and a nitrogen cold atmosphere (−50 °C). Data collection and integration were performed using SMART APEX3 (Bruker, 2016) and SAINT (Bruker, 2016), and absorption correction was performed using a multiscan method implemented in SADABS (Bruker, 2002). The structure was analyzed and refined via the full-matrix least-squares method on F^2 using SHELXTL (University of Göttingen, Göttingen, Germany).

In order to check whether the peak obtained from the DSC result is T_C or a melting temperature T_m, it was observed using a polarizing optical microscope (Carl Zeiss, Oberkochen, Germany) with a THMS600 heating stage (Linkam, Salfords, UK) at an appropriate temperature for a single crystal.

NMR spectroscopy of the $[NH_3(CH_2)_5NH_3]MnCl_4$ crystals was conducted using a 400 MHz Avance II+ solid NMR spectrometer (Bruker) with a 4 mm magic angle spinning (MAS) probe (Western Seoul Center, KBSI). ^1H and ^{13}C MAS NMR spectra were recorded at Larmor frequencies of 400.13 and 100.61 MHz, respectively. The MAS speed used to minimize the spinning sideband overlap was 10 kHz, and NMR chemical shifts were calibrated using tetramethylsilane (TMS) as the standard. The ^1H and ^{13}C $t_{1\rho}$ values were obtained via the $\pi/2 - \tau$ sequence method by changing the spin-locking pulses—the $\pi/2$ pulse widths for ^1H and ^{13}C were ~3.7 µs. The temperature variation was determined by adjusting the heater current and N_2 gas flow.

3. Results

3.1. FT-IR Spectroscopy

Figure 2 shows the FT-IR spectrum of the $[NH_3(CH_2)_5NH_3]MnCl_4$ crystal at 300 K in the range 4000–500 cm^{-1}. The bands at 3122 and 3043 cm^{-1} are characteristic of the C–H bonds of the protonated ligand, and the band at 2934 cm^{-1} suggests the presence of $N-H\cdots Cl$ hydrogen bonds. The band at 1568 cm^{-1} is due to the asymmetric mode of NH_3, whereas the strong band at 1488 cm^{-1} is assigned to the symmetric deformation mode of NH_3. Finally, the bands close to 1169 and 980 cm^{-1} are assigned to the C–N and C–C modes, respectively. The observed FT-IR bands are consistent with those previously reported [23].

3.2. Phase Transition and Crystal Structure

The DSC thermogram measured at a heating rate of 10 K min^{-1} under an N_2 atmosphere is shown in Figure 3. An endothermic peak is observed at 298 K, and the T_C of 298 K is consistent with that reported previously [36]. The enthalpy for the phase transition was 689 J/mol.

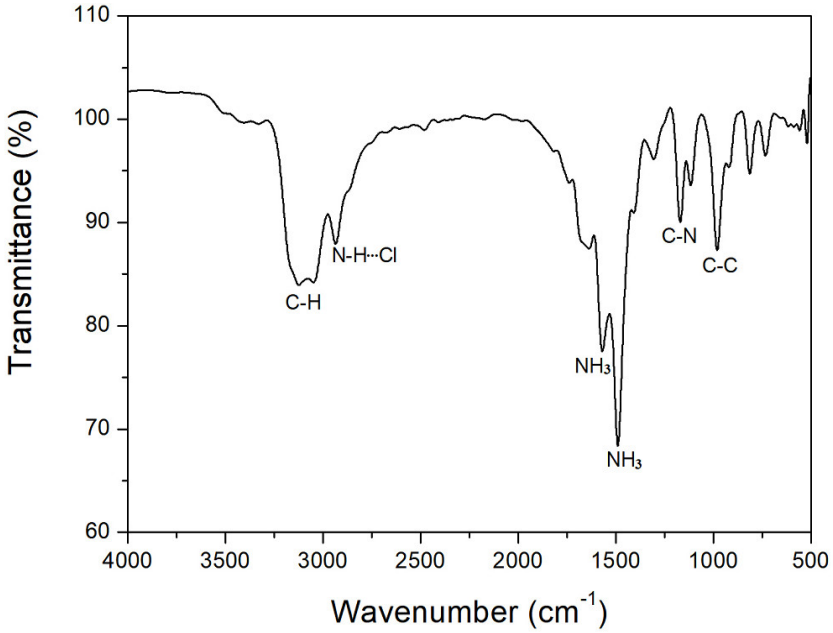

Figure 2. FT–IR spectrum of $[NH_3(CH_2)_5NH_3]MnCl_4$ at 300 K.

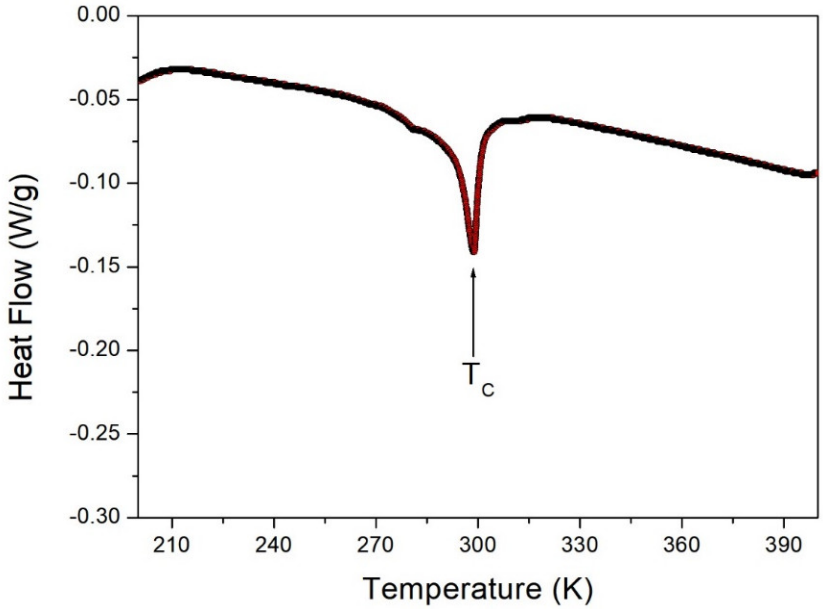

Figure 3. Differential scanning calorimetry curve of $[NH_3(CH_2)_5NH_3]MnCl_4$.

The structures obtained via single-crystal XRD are identical to the orthorhombic structures below T_C and above T_C. The lattice constants at 173 K (<T_C) are a = 24.1756 Å, b = 7.1535 Å, and c = 7.3314 Å in the space group Imma, whereas those at 333 K (>T_C) are a = 23.9162 Å, b = 7.1877 Å, and c = 7.3898 Å in the space group Imma. Table 1 shows the single-crystal data collection and refinement parameters of the $[NH_3(CH_2)_5NH_3]MnCl_4$ crystal at 173 and 333 K, and the atomic numbering scheme and thermal ellipsoids of the H atoms are shown in Figure 4. The Mn atom is coordinated to six Cl atoms, forming an almost regular octahedron, $MnCl_6$, and the six N-linked hydrogen atoms in one formula unit form N−H···Cl hydrogen bonds. The lattice constants as functions of temperature are shown in Figure 5. The lattice constants do not change at ~T_C, and it does not appear to be significantly related to the T_C. The detailed results of XRD of the crystal structure are shown in the Supplementary Information S1 and S2.

Table 1. Crystal data and structure refinement for $[NH_3(CH_2)_5NH_3]MnCl_4$ at 173 K and 330 K. The full data are available in the CIF files.

Chemical Formula	$\mathbf{C_5H_{16}N_2MnCl_4}$	$\mathbf{C_5H_{16}N_2MnCl_4}$
Weight	300.94	300.94
Crystal system	Orthorhombic	Orthorhombic
Space group	Imma	Imma
T (K)	173	330
a (Å)	24.1756	23.9162
b (Å)	7.1535	7.1877
c (Å)	7.3314	7.3898
Z	4	4
V (Å^3)	1267.89	1270.32
Radiation type	Mo-Kα	Mo-Kα
Wavelength (Å)	0.71073	0.71073
Reflections collected	5418	5258
Independent reflections	867	863
Goodness of fit on F^2	1.070	1.118
Final *R* indices [I > 2sigma(I)]	R_1 = 0.0383, wR_2 = 0.1178	R_1 = 0.0312, wR_2 = 0.0957
R indices (all data)	R_1 = 0.0394, wR_2 = 0.1190	R_1 = 0.0330, wR_2 = 0.0974

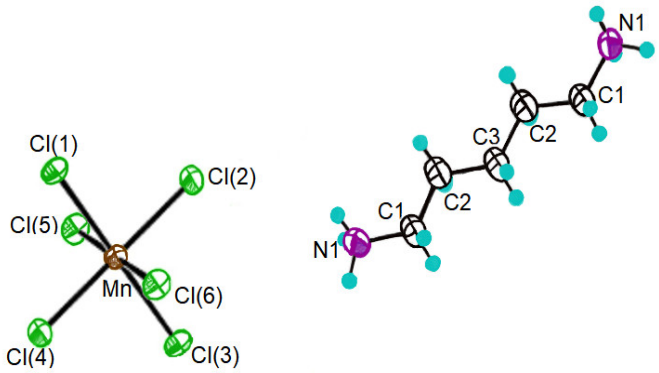

Figure 4. Thermal ellipsoid plot (50% probability) for structure of $[NH_3(CH_2)_5NH_3]MnCl_4$ at 300 K.

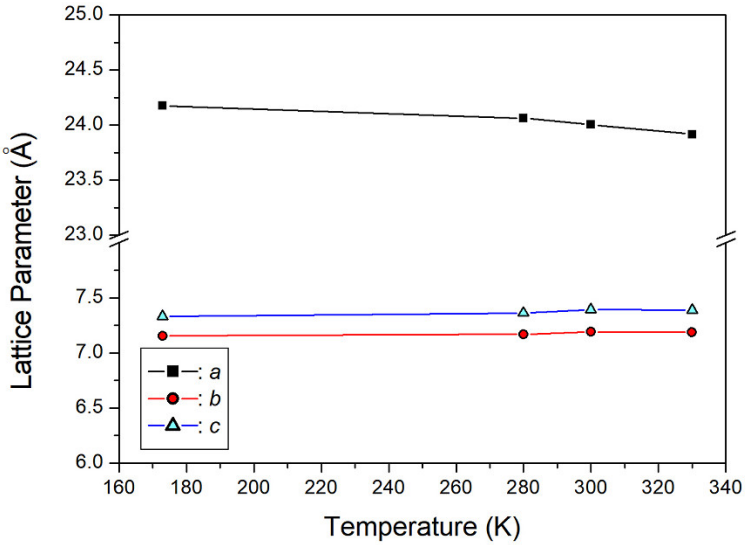

Figure 5. Single-crystal XRD parameters of a $[NH_3(CH_2)_5NH_3]MnCl_4$ crystal at 173, 280, 300 and 333 K.

3.3. Thermodynamic Properties

To determine whether the endothermic peaks were related to phase transitions or decomposition, TGA and differential thermal analysis (DTA) were performed at the same heating rate as that used during DSC. The TGA and DTA thermograms shown in Figure 6 reveal that the crystals are virtually stable up to approximately 570 K. The molecular weight of $[NH_3(CH_2)_5NH_3]MnCl_4$ decreases with increasing temperature above 570 K, and the amount of residue based on the total molecular weight is obtained using Equation (1) [37,38]:

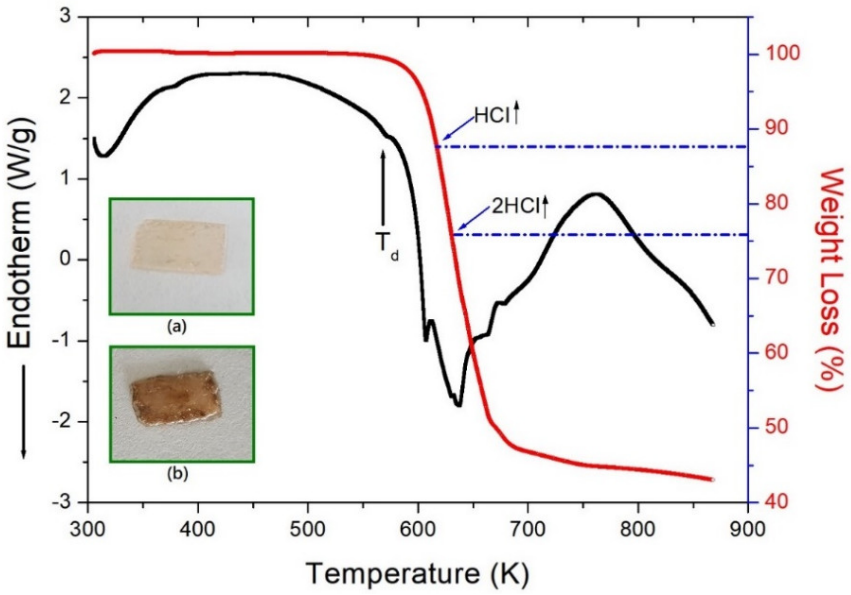

Figure 6. Thermogravimetric analysis and differential thermal analysis curves of $[NH_3(CH_2)_5NH_3]MnCl_4$ (Inset: Changes in crystal by optical polarizing microscopy at (**a**) 300 K and (**b**) 617 K).

1st step

$$[NH_3(CH_2)_5NH_3]MnCl_4 \text{ (MW: 300.94 g)} \rightarrow [NH_2(CH_2)_5NH_2{\cdot}2HCl]MnCl_2$$

$$\rightarrow [NH_2(CH_2)_5NH_2{\cdot}HCl]MnCl_2 \text{ (s)} + HCl \text{ (g)}$$

Residue:

$$[NH_2(CH_2)_5NH_2{\cdot}HCl]MnCl_2 \text{ (s)}/[NH_3(CH_2)_5NH_3]MnCl_4 = 87.88\%$$

2nd step:

$$[NH_3(CH_2)_5NH_3]MnCl_4 \rightarrow [NH_2(CH2)_5NH_2{\cdot}2HCl]MnCl_2$$

$$\rightarrow [NH_2(CH2)_5NH_2]MnCl_2 \text{ (s)} + 2HCl \text{ (g)}$$

Residue:

$$[NH_2(CH_2)_5NH_2]MnCl_2 \text{ (s)}/[NH_3(CH_2)_5NH_3]MnCl_4 = 75.77\% \quad (1)$$

The temperature at which mass loss commences, based on the TGA thermogram, is approximately 570 K. Therefore, 570 K is the partial thermal decomposition temperature T_d. Mass losses of approximately 12% and 24% close to 617 and 630 K may be attributed to the loss of HCl and 2HCl, respectively, as shown in Figure 6. The molecular weight of the crystal decreases sharply between 600 and 700 K, with a mass loss of 50% at approximately 700 K.

To verify the results of TGA and DSC, a single crystal was observed using a polarizing optical microscope while varying the temperature. At 300 K, the crystal is transparent

and light yellow, as shown in Figure 6a. The crystal turns slightly opaque at ~580 K due to partial thermal decomposition. Upon heating further to 617 K, HCl is eliminated, the crystal turns brown, and the surface also appears to melt slightly, as shown in Figure 6b. Based on the results of DSC, TGA, and polarizing microscopy, T_C = 298 K, as shown in the DSC, whereas T_d = 570 K.

3.4. ^1H and ^{13}C NMR Chemical Shifts

The ^1H MAS NMR spectra of the $[NH_3(CH_2)_5NH_3]MnCl_4$ crystals recorded at ~T_C are shown in Figure 7. The observed resonance lines at low temperatures are asymmetric because of the overlap of the signals representing NH_3 and CH_2. The linewidths A and B on the left- and right-hand sides of the half-maximum shown in Figure 7 are not equal. Above 300 K, the NH_3 and CH_2 signals are resolved, and the respective chemical shifts of the resonance lines of NH_3 and CH_2 are observed at 9.29 and 2.89 ppm. The spinning sidebands are marked with "+" and "o" to represent ^1H in NH_3 and CH_2, respectively. The ^1H chemical shifts of CH_2 do not vary significantly at ~T_C, whereas changes in the ^1H chemical shifts of NH_3 are observed at ~T_C. The larger changes in the ^1H NMR chemical shifts of NH_3 compared to those in the ^1H NMR chemical shifts of CH_2 at ~T_C suggest a change in the N−H···Cl hydrogen bonding between Cl around Mn and H of NH_3.

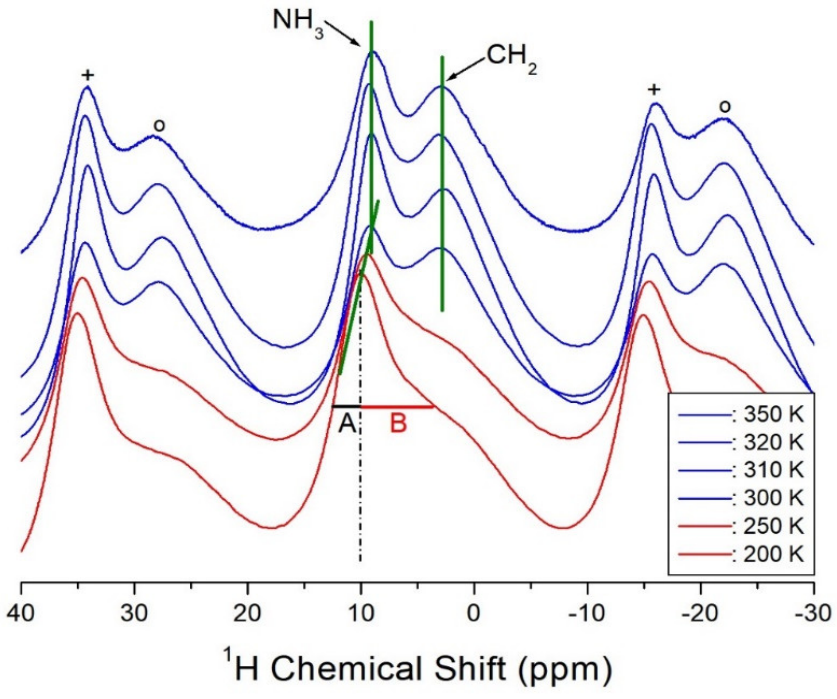

Figure 7. ^1H NMR chemical shifts of $[NH_3(CH_2)_5NH_3]MnCl_4$ at 200, 250, 300, 310, 320, and 350 K. + and o are the spinning sidebands.

In addition, the ^{13}C NMR chemical shifts in the MAS NMR spectra of CH_2 in $[NH_3(CH_2)_5NH_3]MnCl_4$ were recorded at ~T_C. The ^{13}C signal of TMS was observed at 38.3 ppm at 300 K, and thus, 38.3 ppm was set as the origin for the ^{13}C chemical shifts. Here, C3 in the $[NH_3(CH_2)_5NH_3]$ cation is located at the center of the cation, C1 is located adjacent to the NH_3 in the cation, and C2 is located between C1 and C3, as shown in the inset of Figure 8. The respective chemical shifts of C1, C2, and C3 at 300 K are observed at 113.44, 88.92 and 80.96 ppm, as shown in Figure 8. The ^{13}C chemical shifts of C1 do not vary significantly at ~T_C, whereas those of C2 and C3 vary at ~T_C.

3.5. ^1H and ^{13}C NMR Spin-Lattice Relaxation Times

The ^1H and ^{13}C MAS NMR method has a very important for understanding the local dynamics. The spin-lattice relaxation times $T_{1\rho}$ for ^1H and ^{13}C in the rotating frame are the

important experiment for studying the dynamical processes. By studying the relaxation of the nuclei in different environments within the cation, it is possible to obtain a detailed picture of the motions. The $T_{1\rho}$ relaxation parameters are particularly informative since it is directly related to those motions in the low- to mid-kHz frequency range [39–41].

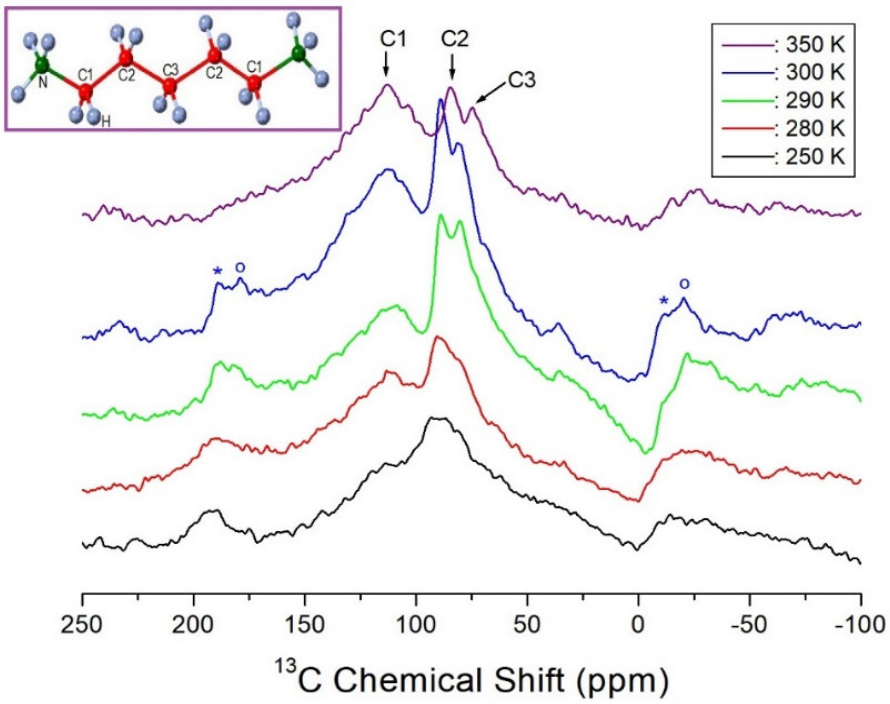

Figure 8. ^{13}C NMR chemical shifts of $[NH_3(CH_2)_5NH_3]MnCl_4$ at 250, 280, 290, 300, and 350 K. * and o are the spinning sidebands.

The ^1H and ^{13}C MAS NMR spectra were acquired at several delay times at each temperature. The relationship between the intensities of the NMR signals and delay time is represented by an exponential function. The magnetization decay rates for protons and carbon are characterized by $t_{1\rho}$ as follows [42,43]:

$$P(\tau)/P(0) = \exp(-\tau/t_{1\rho}), \quad (2)$$

where $P(\tau)$ and $P(0)$ are the NMR signal intensities at τ and $\tau = 0$, respectively. The ^1H and ^{13}C NMR spectra of $[NH_3(CH_2)_5NH_3]MnCl_4$ were recorded with various time delays. The decay curves may be represented by a single exponential function, as shown in Equation (2). However, the ^1H $t_{1\rho}$ values of NH_3 and CH_2 at low temperatures may not be distinguished because of the overlapping ^1H NMR signals. The ^1H $t_{1\rho}$ values depend highly on the temperature, as shown in Figure 9. The ^1H $t_{1\rho}$ values of CH_2 and NH_2 display significant changes at ~T_C, indicating that the ^1H energy transfer of CH_2 and NH_3 changes significantly. Moreover, the ^{13}C $t_{1\rho}$ values of C1, C2, and C3 are obtained from the slopes of their recovery traces. The ^{13}C $t_{1\rho}$ values of C1, C2, and C3 at ~T_C are virtually continuous. Notably, the $t_{1\rho}$ values of C1, which are adjacent to NH_3, are the shortest. The low $t_{1\rho}$ values of C1, which are close to the Mn^{2+} ions, are related to the magnetic moments of the Mn^{2+} ions, which are paramagnetic.

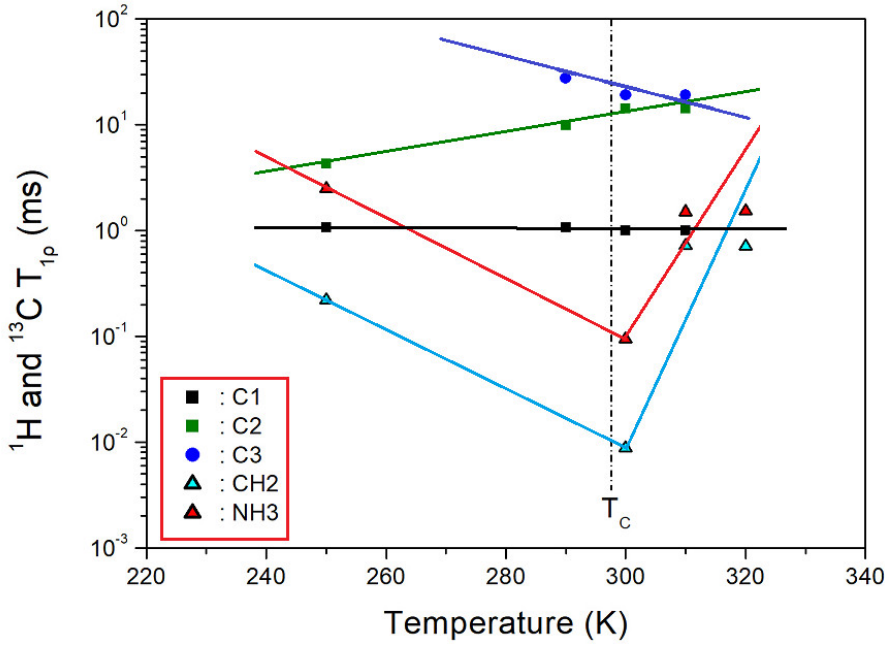

Figure 9. Spin-lattice relaxation times $t_{1\rho}$ for ^{1}H and ^{13}C of $[NH_3(CH_2)_5NH_3]MnCl_4$ near T_C.

4. Discussion

The crystal structures, phase transitions, thermal stabilities, and molecular dynamics of the $[NH_3(CH_2)_5NH_3]MnCl_4$ crystals were investigated using XRD, DSC, TGA, and NMR spectroscopy. First, we reconfirmed that the structure was an orthorhombic system in the space group Imma at 173 and 330 K, and Table 2 shows our results and those previously reported. Arend et al. suggested the space group as Ima2 or Imma at ~T_C [34,35], and Chhor et al. [31] reported that the structure was orthorhombic in the space groups Pnma below T_C and Imma above T_C. According to Lv et al. [36], the space groups below T_C and above T_C were Pnma and Imma, respectively, and Modal et al. [23] reported that the space group at T_C, not below T_C or above T_C, was $I2_12_12_1$. In this study, the space group and lattice parameters of the crystal structure differ slightly, and thus, to study the phase transition, an accurate structural analysis is required. Our results are similar to those above T_C reported by Lv et al. [36].

Table 2. Phase transition temperature T_C (K), structure, space group, lattice constants (Å), Z, and measured temperature (K) for $[NH_3(CH_2)_5NH_3]MnCl_4$ crystal.

	Arend et al.	**Chhor et al.**		**Lv et al.**		**Mondal et al.**	**Present Work**	
T_C	301	299.6		298			298	
Structure	Orthor.	Orthor.	Orthor.	Orthor.	Orthor.	Orthor.	Orthor.	Orthor.
Space group	Ima2 or Imma	Pnma	Imma	Pnma	Imma	$I2_12_12_1$	Imma	Imma
Lattice constants	a = 7.152			a = 7.149	a = 23.94	a = 7.1742	a = 24.1756	a = 23.9162
	b = 7.360			b = 24.171	b = 7.191	b = 7.3817	b = 7.1535	b = 7.1877
	c = 23.986			c = 7.334	c = 7.399	c = 23.9650	c = 7.3314	c = 7.3898
Z	4	4	2	4	4	4	4	4
Measured Temperature	At room temp.	299.6 < T_C	299.6 > T_C	173	333	298	173	333
Reference	[34,35]	[31]	[31]	[36]	[36]	[23]		

Our results showed that the thermal stability was relatively high, with a thermal decomposition temperature of approximately 570 K. The NMR spectra further suggested

that the energy transfer of ^{1}H at ~T_C was very large, as indicated by the large thermal displacement around the ^{1}H atoms.

5. Conclusions

As previously reported by other groups, the space groups under T_C were Pnma or $I2_12_12_1$. Thus, we analyzed Pnma and $I2_12_12_1$ by XRD results, but determined to be closer to Imma. Based on the results of XRD, the structures below T_C and above T_C were orthorhombic in the space group Imma. There may be several reasons for the slightly different results. T_C is 298 K, and thus, the temperature required to characterize the structure should be accurately determined. The difference in the single crystal structure may be due to the observed temperature difference, and it is thought that it may be slightly different depending on the crystal growth conditions; a single crystal may be grown into a naturally occurring structure or a single crystal having a new structure depending on temperature, which is one of the growth conditions. For example, the direction of the twin domain wall in the case of $BiVO_4$ having a ferroelastic twin structure was different [44]. The phase transition at 298 K is due to the energy transfer of ^{1}H, with no structural change. The influences of the chemical shifts of ^{1}H of NH_3 and short molecular weight of C1 adjacent to NH_3 in the $[NH_3(CH_2)_5NH_3]MnCl_4$ crystal were insignificant, indicating a minor change in the N−H···Cl hydrogen bond related to the coordination geometry of the $MnCl_6$ anion. The structural phenomenon revealed by XRD and NMR at ~T_C shows the potential for the realization of solar cells for use in various applications.

Supplementary Materials: The following supporting information can be downloaded at: https://www.mdpi.com/article/10.3390/cryst12091298/s1, Table S1: Crystal data and structure refinement for Imma_a; Table S2: Atomic coordinates ($\times 10^4$) and equivalent isotropic displacement parameters (Å^2 $\times$ 10^3) for Imma_a; Table S3: Bond length [Å] and angle [°] for Imma_a; Table S4: Anisotropic displacement parameters (Å^2 $\times$ 10^3) for Imma_a; Table S5: Hydrogen coordinates ($\times 10^4$) and isotropic displacement parameters (Å^2 $\times$ 10^3) for Imma_a.

Author Contributions: A.R.L. designed the project and performed X-ray and NMR experiments. Y.N. performed DSC, TGA, and optical polarizing microscope experiments. All authors have read and agreed to the published version of the manuscript.

Funding: This research was supported by the Basic Science Research Program of the National Research Foundation of Korea, which is funded by the Ministry of Education, Science, and Technology (2018R1D1A1B07041593, 2016R1A6A1A03012069).

Data Availability Statement: Not applicable.

Conflicts of Interest: The authors declare that they have no known competing financial interests or personal relationships that could have appeared to influence the work reported in this paper.

References

1. Zhang, Z.X.; Su, C.-Y.; Li, J.; Song, X.-J.; Fu, D.-W.; Zhang, Y. Ferroelastic Hybrid Bismuth Bromides with Dual Dielectric Switches. *Chem. Mater.* **2021**, *33*, 5790–5799. [CrossRef]
2. Su, C.-Y.; Yao, Y.-F.; Zhang, Z.-X.; Wang, Y.; Chen, M.; Huang, P.-Z.; Zhang, Y.; Qiao, W.-C.; Fu, D.-W. The construction of a two-dimensional organic–inorganic hybrid double perovskite ferroelastic with a high T_c and narrow band gap. *Chem. Sci.* **2022**, *13*, 4794–4800. [CrossRef] [PubMed]
3. Shao, T.; Gong, J.M.; Liu, J.; Han, L.J.; Chen, M.; Jia, Q.; Fu, D.W.; Lu, H.-F. 2D lead-free organic–inorganic hybrid exhibiting dielectric and structural phase transition at higher temperatures. *CrystEngComm* **2022**, *24*, 4346–4350. [CrossRef]
4. Hermes, I.M.; Bretschneider, S.A.; Bergmann, V.W.; Klasen, D.; Mars, J.; Tremel, W.; Laquai, F.; Butt, H.-J.; Mezger, M.; Berger, R.; et al. Ferroelastic Fingerprints in Methylammonium Lead Iodide Perovskite. *J. Phys. Chem. C* **2016**, *120*, 5724–5731. [CrossRef]
5. Strelcov, E.; Dong, Q.; Li, T.; Chae, J.; Shao, Y.; Deng, Y.; Gruverman, A.; Huang, J.; Centrone, A. $CH_3NH_3PbI_3$ perovskites: Ferroelasticity revealed. *Sci. Adv.* **2017**, *3*, e1602165. [CrossRef] [PubMed]
6. Liu, Y.; Collins, L.; Proksch, R.; Kim, S.; Watson, B.R.; Doughty, B.; Calhoun, T.R.; Ahmadi, M.; Ievlev, A.V.; Jesse, S.; et al. Chemical nature of ferroelastic twin domains in $CH_3NH_3PbI_3$ perovskite. *Nat. Mater.* **2018**, *17*, 1013–1019. [CrossRef] [PubMed]
7. Zang, W.; Xiong, R.-G. Ferroelectric Metal–Organic Frameworks. *Chem. Rev.* **2012**, *112*, 1163–1195. [CrossRef]

8. Lim, A.R.; Kwac, L.K. Advances in physicochemical characterization of lead-free hybrid perovskite $[NH_3(CH_2)_3NH_3]CuBr_4$ crystals. *Sci. Rep.* **2022**, *12*, 8769. [CrossRef]
9. Su, C.; Lun, M.; Chen, Y.; Zhou, Y.; Zhang, Z.; Chen, M.; Huang, P.; Fu, D.; Zhang, Y. Hybrid Optical-Electrical Perovskite Can Be a Ferroelastic Semiconductor. *CCS Chem.* **2021**, *4*, 2009–2019. [CrossRef]
10. Xie, Y.; Ai, Y.; Zeng, Y.-L.; He, W.-H.; Huang, X.-Q.; Fu, D.-W.; Gao, J.-X.; Chen, X.-G.; Tang, Y.-Y.; Am, J. The Soft Molecular Polycrystalline Ferroelectric Realized by the Fluorination Effect. *Chem. Soc.* **2020**, *142*, 12486–12492. [CrossRef]
11. Fu, D.-W.; Gao, J.-X.; He, W.-H.; Huang, X.-Q.; Liu, Y.-H.; Al, Y. High-T_c Enantiomeric Ferroelectrics Based on Homochiral Dabco-derivatives (Dabco=1,4-Diazabicyclo [2.2.2]octane). *Angew. Chem. Int. Ed.* **2020**, *59*, 17477–17481. [CrossRef] [PubMed]
12. Knop, O.; Wasylishen, R.E.; White, M.A.; Cameron, T.S.; Van Oort, M.J.M. Alkylammonium lead halides. Part 2. $CH_3NH_3PbX_3$ (X = Cl, Br, I) perovskites: Cuboctahedral halide cages with isotropic cation reorientation. *Can. J. Chem.* **1990**, *68*, 412–422. [CrossRef]
13. Chen, Q.; Marco, N.D.; Yang, Y.; Song, T.-B.; Chen, C.-C.; Zhao, H.; Hong, Z.; Zhou, H.; Yang, Y. Under the spotlight: The organic–inorganic hybrid halide perovskite for optoelectronic applications. *Nano Today* **2015**, *10*, 355–396. [CrossRef]
14. Abdel-Aal, S.K.; Abdel-Rahman, A.S.; Kocher-Oberlehner, G.G.; Ionov, A.; Mozhchil, R. Structure, optical studies of two-dimensional hybrid perovskite for photovoltaic applications. *Acta Cryst.* **2017**, *73*, C1116. [CrossRef]
15. Mostafa, M.F.; Elkhiyami, S.S.; Alal, S.A. Discontinuous transition from insulator to semiconductor induced by phase change of the new organic-inorganic hybrid $[(CH_2)_7(NH_3)_2]CoBr_4$. *Mater. Chem. Phys.* **2017**, *199*, 454–463. [CrossRef]
16. Milic, J.V.; Im, J.-H.; Kubicki, D.J.; Ummadisingu, A.; Seo, J.-Y.; Li, Y.; Ruiz-Preciado, M.A.; Dar, M.I.; Zakeeruddin, S.M.; Emsley, L.; et al. Supramolecular Engineering for Formamidinium-Based Layered 2D Perovskite Solar Cells: Structural Complexity and Dynamics Revealed by Solid-State NMR Spectroscopy. *Adv. Energy Mater.* **2019**, *9*, 1900284. [CrossRef]
17. Rao, C.N.R.; Cheetham, A.K.; Thirumurugan, A. Hybrid inorganic–organic materials: A new family in condensed matter physics. *J. Phys. Condens. Matter* **2008**, *20*, 83202. [CrossRef]
18. Cheng, Z.; Lin, J. Layered organic–inorganic hybrid perovskites: Structure, optical properties, film preparation, patterning and templating engineering. *CrystEngComm* **2010**, *12*, 2646–2662. [CrossRef]
19. Mostafa, M.F.; El-khiyami, S.S. Crystal structure and electric properties of the organic–inorganic hybrid: $[(CH_2)_6(NH_3)_2]ZnCl_4$. *J. Solid State Chem.* **2014**, *209*, 82–88. [CrossRef]
20. Gonzalez-Carrero, S.; Galian, R.E.; Perez-Prieto, J. Organometal Halide Perovskites: Bulk Low-Dimension Materials and Nanoparticles. *Part. Syst. Charact.* **2015**, *32*, 709–720. [CrossRef]
21. Abdel-Adal, S.K.; Kocher-Oberlehner, G.; Ionov, A.; Mozhchil, R.N. Effect of organic chain length on structure, electronic composition, lattice potential energy, and optical properties of 2D hybrid perovskites $[(NH_3)(CH_2)_n(NH_3)]CuCl_4$, n = 2–9. *Appl. Phys. A* **2017**, *123*, 531. [CrossRef]
22. Liu, W.; Xing, J.; Zhao, J.; Wen, X.; Wang, K.; Peixiang, L.; Xiong, Q. Giant Two-Photon Absorption and Its Saturation in 2D Organic–Inorganic Perovskite. *Adv. Opt. Mater.* **2017**, *5*, 1601045. [CrossRef]
23. Mondal, P.; Abdel-Aal, S.K.; Das, D.; Manirul Islam, S.K. Catalytic Activity of Crystallographically Characterized Organic–Inorganic Hybrid Containing 1,5-Di-amino-pentane Tetrachloro Manganate with Perovskite Type Structure. *Cat. Lett.* **2017**, *147*, 2332–2339. [CrossRef]
24. Elseman, A.M.; Shalan, A.E.; Sajid, S.; Rashad, M.M.; Hassan, A.M.; Li, M. Copper-Substituted Lead Perovskite Materials Constructed with Different Halides for Working $(CH_3NH_3)_2CuX_4$-Based Perovskite Solar Cells from Experimental and Theoretical View. *ACS Appl. Mater. Interfaces* **2018**, *10*, 11699–11707. [CrossRef]
25. Aramburu, J.A.; Garcia-Fernandez, P.; Mathiesen, N.R.; Garcia-Lastra, J.M.; Moreno, M. Changing the Usual Interpretation of the Structure and Ground State of Cu^{2+}-Layered Perovskites. *J. Phys. Chem. C* **2018**, *122*, 5071–5082. [CrossRef]
26. Abdel-Aal, S.K.; Ouasri, A. Crystal structure, Hirshfeld surfaces and vibrational studies of tetrachlorocobaltate hybrid perovskite salts $NH_3(CH_2)_nNH_3CoCl_4$ (n = 4, 9). *J. Mol. Struct.* **2022**, *1251*, 131997. [CrossRef]
27. Abdel, S.K.; Abdel-Rahman, A.S.; Gamal, W.M.; Abdel-Kader, M.; Ayoub, H.S.; El-Sherif, A.F.; Kandeel, M.F.; Bozhko, S.; Yakimov, E.E.; Yakimov, E.B. Crystal structure, vibrational spectroscopy and optical properties of a one-dimensional organic–inorganic hybrid perovskite of $[NH_3CH_2CH(NH_3)CH_2]BiCl_5$. *Acta Cryst.* **2019**, *75*, 880–886. [CrossRef]
28. Guillaume, F.; Sourisseau, C.; Lucazeau, G.; Dianoux, A.J. Reorientational motions and phase transitions in some perovskite type layered compounds $[NH_3(CH_2)_nNH_3]MnCl_4$, n = 3, 5, in Dynamics of molecular crystals. In Proceedings of the 41st International Meeting on Physical Chemistry, Grenoble, France, 30 June–4 July 1986; p. 173.
29. Guillaume, F.; Sourisseau, C.; Dianoux, A.J. Molecular motions in perovskite type layered compounds $[NH_3(CH_2)_nNH_3]MnCl_4$, with n = 3, 4, 5; an incoherent neutron scattering study. *Physica B* **1989**, *156*, 359–362. [CrossRef]
30. Negrier, P.; Couzi, M.; Chanh, N.B.; Hauw, C.; Meresse, A. Structural phase transitions in the perovskite-type layer compound $NH_3(CH_2)_5NH_3CdCl_4$. *J. Phys. Fr.* **1989**, *50*, 405–430. [CrossRef]
31. Chhor, K.; Abello, L.; Pommier, C.; Sourisseau, C. Reorientational motions in a perovskite-type layer compound $[NH_3(CH_2)_5NH_3]MnCl_4$. A calorimetric study. *J. Phys. Chem. Solids* **1988**, *49*, 1079–1085. [CrossRef]
32. Lim, A.R.; Kim, S.H. Physicochemical Property Investigations of Perovskite-Type Layer Crystals $[NH_3(CH_2)_nNH_3]CdCl_4$ (n = 2, 3, and 4) as a Function of Length n of CH_2. *ACS Omega* **2021**, *6*, 27568–27577. [CrossRef] [PubMed]
33. Rong, S.-S.; Faheem, M.B.; Li, Y.-B. Perovskite single crystals: Synthesis, properties, and applications. *J. Electron. Sci. Technol.* **2021**, *19*, 100081. [CrossRef]

34. Arend, H.; Granicher, H. On phase transitions in chloride perovskite layer structures. *Ferroelectrics* **1976**, *13*, 537–539. [CrossRef]
35. Arend, H.; Tichy, K.; Baberschke, K.; Rys, F. Chloride perovskite layer compounds of $[NH_3\text{-}(CH_2)_n\text{-}NH_3]MnCl_4$ formula. *Solid State Commun.* **1976**, *18*, 999–1003. [CrossRef]
36. Lv, X.-H.; Liao, W.-Q.; Li, P.-F.; Wang, Z.-X.; Mao, C.-Y.; Zhang, Y. Dielectric and photoluminescence properties of a layered perovskite-type organic–inorganic hybrid phase transition compound: $NH_3(CH_2)_5NH_3MnCl_4$. *J. Mater. Chem. C* **2016**, *4*, 1881–1885. [CrossRef]
37. Lim, A.R.; Schueneman, G.T.; Novak, B.M. The $T_{1\rho}$ spin-lattice relaxation time of interpenetrating networks by solid state NMR. *Solid State Commun.* **1998**, *109*, 465. [CrossRef]
38. Lim, A.R. Structural characterization, thermal properties, and molecular motions near the phase transition in hybrid perovskite $[(CH_2)_3(NH_3)_2]CuCl_4$ crystals: ^1H, ^{13}C, and ^{14}N nuclear magnetic resonance. *Sci. Rep.* **2020**, *10*, 20853. [CrossRef]
39. Mcbrierty, V.J.; Packer, K.J. *Nuclear Magnetic Resonance in Solid Polymers*; Cambridge University Press: Cambridge, UK, 1993.
40. Koenig, J.L. *Spectroscopy of Polymers*; Elsevier: New York, NY, USA, 1999.
41. Harris, R.K. *Nuclear Magnetic Resonance Spectroscopy*; Pitman Pub: London, UK, 1983.
42. Lim, A.R.; Kim, S.H.; Joo, Y.L. Physicochemical properties and structural dynamics of organic–inorganic hybrid $[NH_3(CH_2)_3NH_3]ZnX_4$ (X = Cl and Br) crystals. *Sci. Rep.* **2021**, *11*, 8408. [CrossRef]
43. Abragam, A. *The Principles of Nuclear Magnetism*; Oxford University Press: Oxford, UK, 1961.
44. Lim, A.R.; Choh, S.H.; Jang, M.S. Prominent ferroelastic domain walls in $BiVO_4$ crystal. *J. Phys. Condens. Matter* **1995**, *7*, 7309. [CrossRef]